

# Multi-objective optimization of tapered tubes for crashworthiness by surrogate methodologies

Masoud Asgari\*, Alireza Babaei and Mohammadamin Jamshidi

Faculty of Mechanical Engineering, K.N. Toosi University of Technology, P.O. Box 19395-1999, Tehran, Iran

(Received March 31, 2017, Revised November 9, 2017, Accepted March 17, 2018)

**Abstract.** In this paper, the single and multi-objective optimization of thin-walled conical tubes with different types of indentations under axial impact has been investigated using surrogate models called metamodels. The geometry of tapered thin-walled tubes has been studied in order to achieve maximum specific energy absorption (SEA) and minimum peak crushing force (PCF). The height, radius, thickness, tapered angle of the tube, and the radius of indentation have been considered as design variables. Based on the design of experiments (DOE) method, the generated sample points are computed using the explicit finite element code. Different surrogate models including Kriging, Feed Forward Neural Network (FNN), Radial Basis Neural Network (RNN), and Response Surface Modelling (RSM) comprised to evaluate the appropriation of such models. The comparison study between surrogate models and the exploration of indentation shapes have been provided. The obtained results show that the RNN method has the minimum mean squared error (MSE) in training points compared to the other methods. Meanwhile, optimization based on surrogate models with lower values of MSE does not provide optimum results. The RNN method demonstrates a lower crashworthiness performance (with a lower value of 125.7% for SEA and a higher value of 56.8% for PCF) in comparison to RSM with an error order of  $10^{-3}$ . The SEA values can be increased by 17.6% and PCF values can be decreased by 24.63% by different types of indentation. In a specific geometry, higher SEA and lower PCF require triangular and circular shapes of indentation, respectively.

**Keywords:** multi-objective optimization; energy absorption; crushing force; metamodel; tapered tube; indentation

## 1. Introduction

Thin-walled tubes, as lightweight energy absorbers, have been used to dissipate energy during the crash phenomenon. These tubes convert the kinetic energy of the impact load to the plastic work and prevent the transfer of energy to the occupants. In order to have ideal crushing characteristics, optimization of structures with low weight and high energy absorption capacity is as a great importance. To this end, surrogate-based optimization has been considered as an alternative method to reduce computational cost.

Many numerical, experimental, and theoretical research have been conducted in order to do in-depth study about the thin-walled structures crashworthiness. Pioneering experimental work were carried out by Abramowicz and Joens on squared-section steel alloy structures in order to investigate the different crushing modes, including the symmetric and axisymmetric modes (Abramowicz and Jones 1984). Various geometrical configurations of energy absorbing structure have been considered. Among the different types of cross sections, circular cross sections are more preferable due to the better manufacturability (Nagel 2005). Moreover, some researchers have considered tapered and pyramid shapes instead of cylindrical ones, due to the better

crashworthy abilities (Kim *et al.* 2002, Qi *et al.* 2012).

An innovation in this regard is implementing imperfections including indentations, longitudinal grooves, and various triggering patterns that makes folding easier and improves the crushing characteristics (Zhang *et al.* 2007, Zhang and Huh 2009, Guler *et al.* 2010, Khayat *et al.* 2017). The number, size, and position of these imperfections were investigated in a number of studies (Hosseinipour and Daneshi 2003, Acar *et al.* 2011). Marzbanrad *et al.* (2009) studied the effective influence of imperfections on maximum crash force and the energy absorption capacity of the structure.

Recently, lots of creative and innovation-based studies such as multi-cell tapered energy absorbers and double-walled tubes have been put into action in order to improve energy absorption performance (Azimi and Asgari 2016a, b, Mahmoodi *et al.* 2016). Also, Baykasoğlu *et al.* proposed a multi-objective optimization of circular tubes with graded thickness. They employed finite element to generate metamodels for prediction of accurate optimal results (Baykasoğlu and Baykasoğlu 2016, 2017). Functionally graded thickness (FGT) for obtaining variable stiffness throughout the length of a structure and providing more efficient control of the crashworthiness parameters have been utilized by Baykasoğlu and Cetin (2015).

In numerical analysis, surrogate modelling techniques are mostly applicable to decrease the computational cost. There are a number of studies in which metamodels are integrated with optimization algorithm to achieve an

\*Corresponding author, Ph.D., Professor,  
E-mail: [asgari@kntu.ac.ir](mailto:asgari@kntu.ac.ir)

optimal design. Zhang (Zhang *et al.* 2014), Khalkhali (Khalkhali and Samareh Mousavi 2012), Azimi and Asgari (Azimi and Asgari 2016b) and Vinayagar and Kumar (Vinayagar and Senthil Kumar 2017), utilized Kriging, Feed Forward Neural Network, quadratic, and a new developed method for optimization procedure, respectively. Baroutaji *et al.* presented a multi-objective optimization of short circular tubes subjected to the quasi-static loading. They developed a linear and quadratic surrogate model to obtain optimal values of diameter, width and thickness of the circular tube (Baroutaji *et al.* 2015). Fang *et al.* carried out a comprehensive review for structural crashworthiness optimization. They have discussed some important topics such as design criteria, surrogate models, geometrical configurations and optimization procedures (Fang *et al.* 2017). Due to the direct influence of the surrogate models over the optimization results, comparison of the performance of the various surrogate models with respect to crashworthiness is of great importance. However, there are limited number of research related to the comparison study between different surrogate models for prediction of crashworthiness optimal values, which are similar to the present study.

Motivated by this fact, the present paper aims to provide a comparison study between four types of metamodels, including Kriging, Feed Forward Neural Network (FNN), Radial Basis Neural Network (RNN), and Response Surface Method (RSM). The optimum values of five design variables (thickness, tapered angle, the bottom radius of frustum, height, and the radius of indentation) for energy absorption characteristics are evaluated based on the explicit dynamic finite element code. Moreover, the effect of indentation shape (circular, hexagonal, squared and triangular) on the crushing mode has been investigated. The model has been validated by a theoretical solution as well as experimental and numerical studies available in the literature. Sample points are selected based on the design of the experiment (DOE) Latin Hypercube method. Evolutionary single and multi-objective Genetic Algorithm (GA) are utilized as the optimization method.

## 2. Problem description and finite element modelling

The structure considered in this paper is a tapered tube of circular cross section. The indentation is located in the middle section of the cone edge to increase the value of energy absorption and prevent global buckling (Najafi 2009). As shown in Fig. 1, in the single and multi-optimization sections of this study, the circular shape of indentation is considered, and geometrical variables including thickness  $t$ , tapered angle  $\alpha$ , the bottom radius of frustum  $R$ , height  $H$ , and the radius of indentation  $r$  are studied in order to find optimum values.

Section 4.2.4 of present study is focused on exploring which types of indentations (triangular, squared, hexagonal, and circular) lead to better crushing characteristics. To this end, four tubes with different shapes of indentation and similar geometries have been shown in Fig. 2.

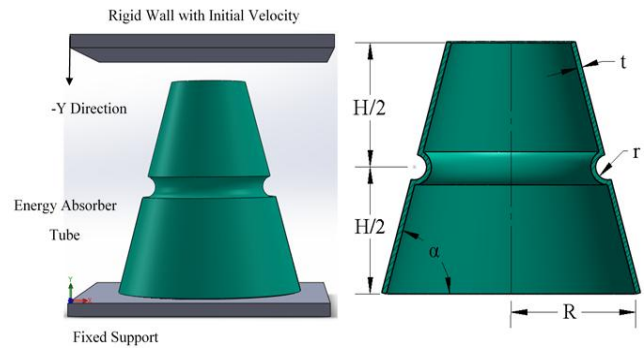


Fig. 1 Schematic of tapered tube under axial crushing.

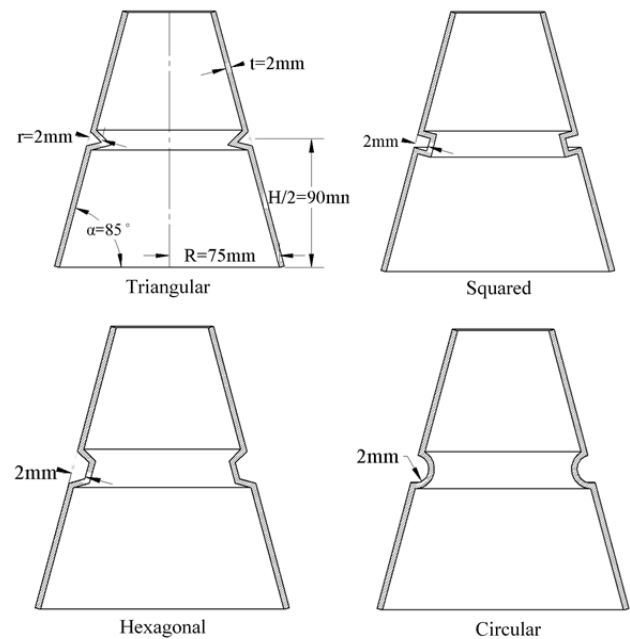


Fig. 2 Tapered tube with different types of indentation.

The performance of the energy-absorbing structure can be evaluated by the means of these two important parameters: specific energy absorption (SEA) and peak crushing force (PCF). The ECR-R29 standard test, in which a pendulum with initial kinematic energy of 30 kJ hits a bumper, is applied to this study. According to the approximate size of an energy-absorbing structure and the length of a vehicle bumper, the initial energy is divided into 20 energy-absorbing structures. For the configuration of boundary conditions, the bottom edge is bonded with a rigid plate.

A 75-kg rigid mass block hits the energy-absorbing structure in the axial direction with initial velocity of  $6.33 \frac{m}{s}$  which provides 1.5 kJ initial kinetic energy for each energy absorber. The schematic of boundary conditions is demonstrated in Fig. 1.

On the other hand, it should be noted that the crushing efficiency would be more useful in the problems that the rigid wall velocity and the length of the tube have constant values in order to can do an existent comparison.

Considering the mentioned design variables, the

Table 1 Strain hardening data for AA 6063T7 (Zhang *et al.* 2010)

Plastic strain	Plastic stress (Mpa)
0	$0.8694 \times 10^2$
$0.2696 \times 10^{-3}$	$0.9594 \times 10^2$
$0.2110 \times 10^{-2}$	$0.1013 \times 10^3$
$0.5746 \times 10^{-2}$	$0.1093 \times 10^3$
$0.1493 \times 10^{-1}$	$0.1273 \times 10^3$
$0.2630 \times 10^{-1}$	$0.1493 \times 10^3$
$0.6939 \times 10^{-1}$	$0.1695 \times 10^3$
0.1527	$0.1710 \times 10^3$

objective functions of the optimization problem are defined as follows

$$\text{Minimize}\{f_1 = -SEA(H, R, t, \alpha, r) \text{ and } f_2 = PCF(H, R, t, \alpha, r)\}$$

An aluminium alloy (AA6063T7 (Zhang *et al.* 2010)) with Young's modulus of 69 Gpa, Poisson's ratio of 0.3, yield strength of 86.94 Mpa, and adensity of  $2700 \text{ kg/m}^3$  is selected. Aluminium alloys are low sensitive to strain rate; therefore, in this study, the effect of strain rate is neglected (Azimi and Asgari 2016a). Based on experimental data in Table 1, the multi-linear hardening curve is assumed as plastic behaviour. Moreover, isotropic hardening and the Von-Mises yield function are considered for the plastic region.

The problem is modelled in the ANSYS Explicit code in a parametric module. In the present study, the Quadrilateral "SHELL 181" element is applied to the energy-absorbing structures. It is a four-node element with six degrees of freedom at each node. The number of integration points is 5, which are located through the thickness of each layer. Two points are located on the top and bottom surfaces, respectively, and the remaining three points are distributed at equal distances between the two points. Two types of contacts are assumed. Firstly, a Line-to-Surface contact is utilized to bond the bottom edge of the tube to the support. Hereafter, automatic contact detection and a frictionless interaction is applied to all components since friction is not the major energy-absorbing mechanism in this problem. The explicit dynamic ANSYS solver uses a central difference time integration scheme, which is often referred to as the Leapfrog method. (ANSYS 2009)

### 2.1 Mesh sensitivity

The mesh sensitivity analysis is carried out to find the appropriate element size for numerical simulations. Since the design space is expanded, the unique element size cannot be obtained in all geometries. Therefore, we consider an element size interval with the average of 10 mm. In order to validate this interval, a set of tapered tubes with different element sizes are simulated. The dimensions of the tubes are similar:  $t = 1 \text{ mm}$ ,  $\alpha = 75$ ,  $R = 125 \text{ mm}$ ,  $r = 6 \text{ mm}$ ,  $H = 250 \text{ mm}$ . Three different element sizes (9, 10, and 12 mm) are considered to examine the numerical convergence and accuracy of interval. The crushing

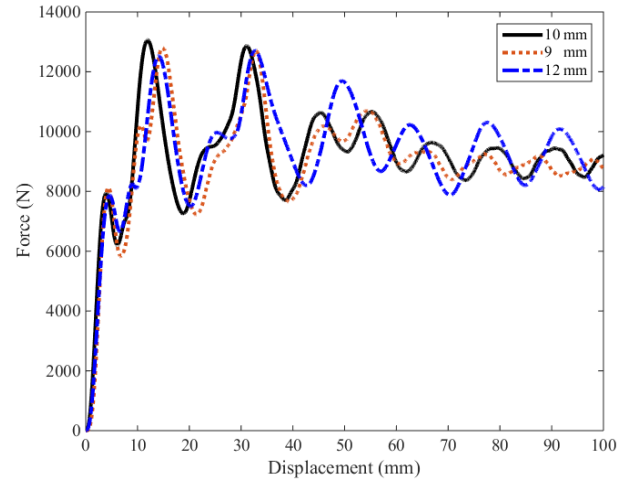


Fig. 3 Mesh sensitivity to force-displacement curve

force versus displacement curves is shown in Fig. 3. It should be noted that the results of tubes with 9 and 10 mm element sizes are similar and to decrease numerical cost we consider element size of 10 mm.

### 2.2 Crashworthiness indices

The performance of energy-absorbing tubes can be evaluated by several indices such as mean crushing force ( $P_{mean}$ ), the PCF, and the SEA. SEA denotes the total absorbed energy of these tubes during the crushing deformation of the structures per unit mass. It can be expressed as follows

$$SEA(\delta) = \frac{\int_0^\delta F(x) dx}{m} \quad (1)$$

where  $F(x)$ ,  $\delta$  and  $m$  are the axial crushing force, the crushing displacement, and the mass of the structure, respectively. Moreover, mean crushing force ( $P_{mean}$ ) can be evaluated based on the value of SEA, and the displacement is expressed as follows

$$P_{mean} = \frac{\text{Energy absorption}}{\delta} \quad (2)$$

### 2.3 Theoretical verification of model

In order to validate results, a comparison is conducted between the finite element analysis and two theoretical solutions. The theoretical solutions are based on a cylindrical thin-walled tube subjected to frontal impact loading with the axisymmetric crushing mode (Ambrosio 2001). According to Fig. 4, during axisymmetric crushing, three plastic hinges are generated. The total plastic energy absorbed by the two plastic hinges that are located at the top and bottom is as follows

$$E_1 = 2\pi RM \quad (3)$$

The plastic collapse moment per unit lateral length for the tube is

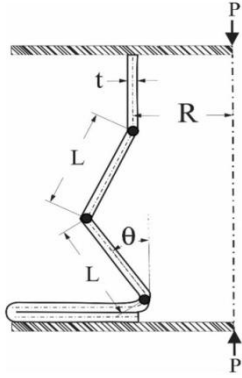


Fig. 4 Axisymmetric crushing mode for an axially compressed cylindrical tube

$$M = \frac{\sqrt{3}}{2} t^2 S_y \quad (4)$$

The energy absorbed by the middle plastic hinge as the position changes from  $R$  to  $R + l$  while the incremental angle  $d\theta$  varies from  $0$  to  $\pi/2$  is as follows

$$E_2 = \int_0^{\pi/2} 4\pi M(R + l \sin\theta) d\theta \quad (5)$$

$$E_2 = 2\pi^2 RM + 4\pi l M \quad (6)$$

Besides, the lateral stretching for hinge lines renders the  $E_3$  energy absorption as the angle varies from  $\theta$  to  $\theta + d\theta$  as follows

$$E_3 = 2\pi S_y l^2 t \quad (7)$$

The total energy absorbed during the generation of one complete wrinkle is  $E_T = E_1 + E_2 + E_3$  and so

$$E_T = \frac{2\pi}{\sqrt{3}} S_y t^2 (\pi R + l) + 2\pi S_y l^2 t \quad (8)$$

Where  $t$ ,  $S_y$ ,  $l$ , and  $R$  are thickness, yield strength, length of the plastic hinge, and radius of the cylinder, respectively. Eqs. (3)-(8) have been considered based on the following reference (Ambrosio 2001).

Moreover, the average crush force of empty tubes can be derived from (Hanssen *et al.* 2000)

$$P_{mean} = k_D S_y (2R)^{1/3} t^{5/3} \quad (9)$$

Where  $k_D$  is a dimensionless constant equal to 17. Using the same parameters for the finite element method, and the theoretical models as  $t = 2.5$  mm,  $S_y = 86.94$  Mpa,  $R = 90$  mm, the total values of energy absorption and mean crushing force by the two methods are illustrated in Table 2.

#### 2.4 Experimental verification of model

The validation of the finite element model is also performed using an experimental test (Zarei and Kröger

Table 2 Theoretical and FEM values for  $EA$  and  $P_{mean}$

	FEM	Refs. (Hanssen <i>et al.</i> 2000)
Energy absorption (J)	1294.2	1143.011
$P_{mean}$ (kN)	34.41	38.43



Fig. 5 Comparison of the deformed shapes between finite element method (FEM) solution and experiment (Zarei and Kröger 2006)

2006). An aluminium tube with material properties are defined in the reference (Zarei and Kröger 2006). From Fig. 5, the deformation patterns are similar in both finite element simulation and experimental result. The force-displacement curves for both the experimental test and the finite element model are provided in Fig. 6. The values of total energy absorption and mean crushing force are also shown in Table 3.

An additional validation for FEM frusta model with the results of Mamalis *et al.* has been made (Mamalis *et al.* 2005). To this end, the aluminum alloy 6061-T6 is considered for the material of energy absorber with a

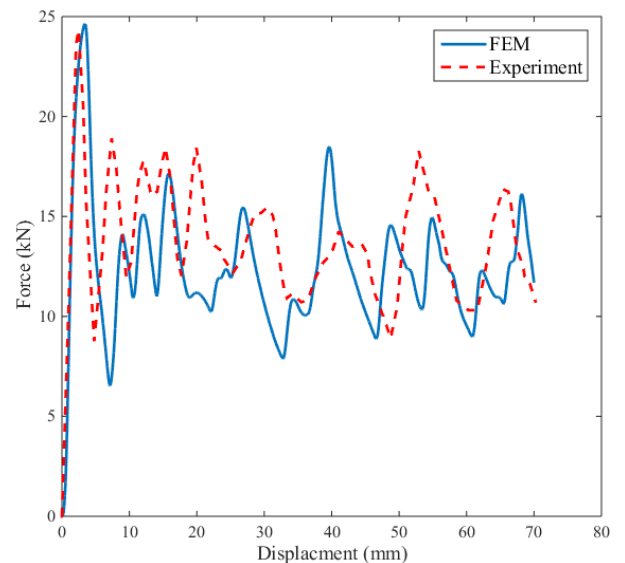
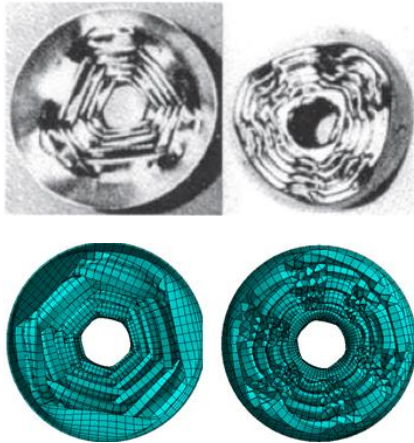


Fig. 6 Force-displacement curves for experimental test (Zarei and Kröger 2006) and finite element solution

Table 3 Experimental (Zarei and Kröger 2006) and FEM values for energy absorption and mean crushing force

	FEM	Experimental
Energy absorption (J)	1000	998
$P_{mean}$ (kN)	11.98	13.03
PCF (kN)	24.70	24.28

Fig. 7 Comparison of the deformed shapes between FEM frusta model and experiment(Mamalis *et al.* 2005)

geometric specifications of a tapered angle ( $\alpha = 10^\circ$ ), height ( $H = 127.1 \text{ mm}$ ), thickness ( $t = 0.48 \text{ mm}$ ) and radius of tapered ( $R = 63.6 \text{ mm}$ ). It should be noted that in the simulation, the crushing condition is considered as a quasi-static and the rigid wall velocity has a constant value during the crushing ( $V = 1 \frac{\text{m}}{\text{s}}$ ). Also, static and dynamic friction coefficient equals to 0.3 and 0.2, respectively. As it is shown in Fig. 7, the deformed shapes of present frusta model are in a good agreement with experimental results. Results of the initial peak force are tabulated in Table 4.

As another validation for frusta, the present frusta model has been compared with those reported by Gupta *et al.* (2006). The Aluminum alloy with multi-linear plastic curve is considered for the material of energy absorber (Yield stress = 55 Mpa, Young's modulus = 70 Gpa, Tangent modulus = 4213 Mpa). The specimen No. C25 with a geometric specifications of semi-apical angle ( $\alpha = 23^\circ$ ), height ( $L = 88.10 \text{ mm}$ ), thickness ( $t = 0.7 \text{ mm}$ ) and base diameter ( $D = 165 \text{ mm}$ ) is chosen to configure the FEM model. It should be noted that in the present simulation, the crushing condition is considered as a quasi-static and the rigid wall velocity has a constant value during the crushing ( $V = 0.1 \frac{\text{m}}{\text{s}}$ ,  $t = 0.1 \text{ sec}$ , crush displacement = 10 mm.).

Table 4 Comparison of experimental (Mamalis *et al.* 2005) and FEM values for frusta initial peak force

	FEM	Experimental (Mamalis <i>et al.</i> 2005)
Initial peak force (kN)	3.09	3.6
Total energy absorption (kJ)	2.14	2.50

Also, static and dynamic friction is considered as 0.1 in this simulation. The Plastic energy absorption and peak initial force of simulated model are 46.5 J and 4.23 kN respectively, while the same parameters reported by Gupta *et al.* are 45 and 4.19 kN. It is clearly found to be a good agreement with results of Gutpa *et al.* (2006).

### 3. Design of experiments and surrogate modelling

#### 3.1 Design of experiments

Design of experiments (DOE) is a strategy to allocate and determine the input data in design space with the aim of maximizing the amount of recognition and having more information on the problem (Park 1994). Within the input data (training sample points), a function or a model is released. These sample points are trained by the surrogate model to predict the demanded responses. In this paper, for the FNN, RNN, and the Kriging surrogate models, the input data is 100 sample points, and the Latin Hypercube

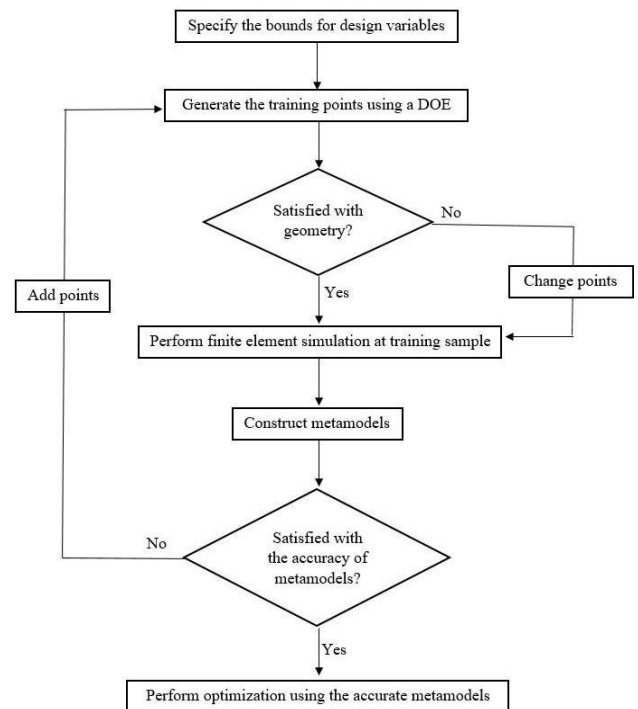


Fig. 8 Process of DOE and optimization using different meta-models

Table 5 Latin Hypercube sample points

point	$H$	$R$	$t$	$\alpha$ ( $^\circ$ )	$r$	SEA (kJ/kg)	PCF (N)
1	151.52	147.42	2.8	83.94	4.34	1.25	175760
2	139.39	123.18	1.99	84.55	7.09	2.46	80559.88
...							
99	309.09	98.94	1.59	79.7	9.76	2.12	50294.32
100	169.23	185	1.94	72.69	7.54	1.42	68307.76

\*Note: All dimensions are in mm

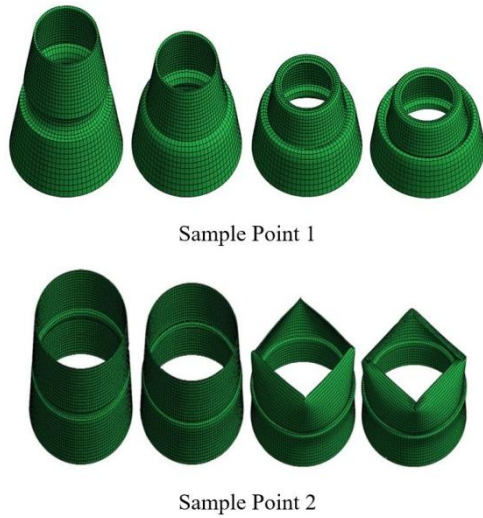


Fig. 9 Deformed shapes of sample points 1 and 2

Sampling (LHS) DOE method is applied. Based on the iterative procedure, we found that the required number of input data points for the second order RSM method is 27. The flowchart of surrogate-based optimization integrated with DOE is shown in Fig. 8. Table 5 and Fig. 9 show the geometry parameters and deformed shapes of sample points 1 and 2 of the following input data. The number of sample points and further details with respect to DOE are provided in Appendix A.

### 3.2 Surrogate modelling

Surrogate modelling is an engineering method that is used when evaluating outputs are not possible because of the complexity of the problem and high computational costs. Meta-models predict responses by means of training sample points, and then training the functions to fit on the input data. In this paper, Kriging, second order RSM, FNN and RNN are utilized for multi-objective and single-objective optimization.

#### 3.2.1 Response surface methodology

One of the engineering methods in surrogate modelling is the 2<sup>nd</sup> order response surface methodology. The following equations demonstrate the quadratic form of this method with respect to the present problem variables (Myers *et al.* 2009)

$$\begin{aligned}
 f(x_1, x_2, x_3, x_4, x_5) \\
 = C_0 + C_1x_1 + C_2x_2 + \dots + C_6x_1^2 + \dots \\
 + C_{11}x_1x_2 + \dots + C_{20}x_4x_5
 \end{aligned} \quad (10)$$

where  $f$  is the predicting function,  $C_i$  are the coefficients and  $x_i$  are the design variables, and  $x_1$  to  $x_5$  are  $H$ ,  $R$ ,  $t$ ,  $\alpha$ , and  $r$ , respectively. After the determination of coefficients, the function is employed in the optimization algorithm. The coefficients are illustrated in Table 6 and the process of coefficient determination is provided in Appendix B. According to Table 6, thickness, tapered

Table 6 Coefficients of RSM method for SEA (kJ/kg) and PCF (N) functions

Coeff.	SEA (kJ/kg)	PCF (N)	Coeff.	SEA (kJ/kg)	PCF (N)
C0	1.91	45.23	C11	0.15	11.80
C1	1.141	11.73	C12	0.65	0.64
C2	1.78	26.72	C13	0.45	10.49
C3	2.11	35.95	C14	0.12	2.28
C4	0.86	31.36	C15	0.94	36.15
C5	0.04	-5.73	C16	0.66	17.51
C6	0.80	4.01	C17	0.01	20.18
C7	0.93	14.23	C18	0.29	37.85
C8	1.13	14.37	C19	0.07	26.68
C9	0.07	28.77	C20	0.03	29.65
C10	0.08	6.03			

radius, and height are important variables for SEA since  $|C_3|$ ,  $|C_2|$ , and  $|C_1|$  have higher magnitudes than other coefficients. Besides, thickness is an effective design variable for the PCF, especially in terms such as  $x_3 \times x_4$  and  $x_3 \times x_2$ .

#### 3.2.2 Radial basis neural network

All the training sample points are implemented in the neural network MATLAB toolbox. The radial basis network type has one layer containing 100 neurons and the spread constant is defined as 1.0. Appendix B provides descriptive details for this section.

#### 3.2.3 Feed forward neural network

In this study, the training sample points are processed by a hidden layer of 10 neurons. All training procedures are performed in the MATLAB Neural Network toolbox with the configuration of Bayesian regularization for the training algorithm. To this end, 70% of sample points are trained, and subsequently, 15% are validated to measure network generalization; the remaining 15% are tested to verify the network performance.

#### 3.2.4 Kriging method

Due to the high accuracy in predicting nonlinear problems, this method has been utilized frequently in recent years (Esfahlani *et al.* 2013, Gu *et al.* 2017). In this method, the target responses are simulated by a major function  $f$  and a residual function  $Z$ . The following equation illustrates the overall form of Kriging formulation (Kozziel *et al.* 2011)

$$s(x) = f(x) + Z(x) \quad (11)$$

All training sample points are implemented in the Dace Kriging toolbox (Lophaven *et al.* 2002). In this study,  $f$  is considered as a 2<sup>nd</sup> order polynomial function and the Gaussian function is used as the correlation. The descriptive details about the Kriging method are included in Appendix B.

## 4. Numerical results

In this part, the fitting quality of surrogate models in training sample points and surrogate-based optimizations using different surrogate models are carried out. Moreover, in the last section, the effects of the indentation's shape are investigated to predict the crushing modes.

### 4.1 Performance of metamodels

The mean squared error (MSE) is selected to demonstrate the differences between approximated outputs (meta-models) and finite element solutions. The MSE values are normalized as follows

$$MSE = \frac{1}{N} \sum_{n=1}^{n=N} (y^{metamodel} - y^{real})^2 \quad (12)$$

$$NMSE = \frac{MSE}{Maximum\ MSE} \quad (13)$$

where  $N$  is the number of training sample points,  $y^{metamodel}$  includes the values of the SEA- and PCF-approximated functions, and  $y^{real}$  refers to finite element solutions. Results for MSE and NMSE in the SEA and the PCF functions are available in Tables 7 and 8.

According to Tables 7 and 8, FNN and RNN have the maximum and the minimum NMSE, respectively. However, RNN, as the most accurate meta-model, does not necessarily lead to global optimum results.

### 4.2 Optimization problems

Single- and multi-objective optimization procedures are performed to maximize the SEA and the PCF. All single- and multi-objective optimization formulations are implemented in the MATLAB optimization toolbox based on the Genetic Algorithm (GA) and the Non-dominated Sorting Genetic Algorithm (NSGA-II), respectively. For single-objective optimization, a population size of 100 and

a convergence tolerance of  $1 \times 10^{-6}$  are assumed. Moreover, in the multi-objective problem, the population size is 300 and the convergence tolerance is constant (as assumed before). For single objective optimization of GA, the algorithm stops if the average relative change in the best fitness function value over maximum generation is less than or equal to function tolerance. For the multi objective optimization of GA, the algorithm stops if the spread, a measurement of the movement of the Pareto front, is equal or less than function tolerance. It is to be noted that in multi objective GA algorithm the spread is a measure of the movement of the points on the Pareto front between the final two iterations.

#### 4.2.1 Single-objective optimization for SEA

Single-objective optimization problem using the mentioned meta-models is formulated as follows

$$\begin{aligned} &\text{Find} && x = (H, R, t, \alpha, r) \\ &\text{Minimize} && f_1 = -SEA(x) \\ &\text{Subjected to:} && \\ &&& 100 \leq H \text{ (mm)} \leq 400 \\ &&& 65 \leq R \text{ (mm)} \leq 185 \\ &&& 0.5 \leq t \text{ (mm)} \leq 3 \\ &&& 60 \leq \alpha \text{ (degree)} \leq 90 \\ &&& 2 \leq r \text{ (mm)} \leq 10 \\ &&& \frac{H}{R} > \tan \alpha \end{aligned}$$

Linear constraints limit the design space to the bounds of design variables and a nonlinear constraint is imposed to form a frustum. Here, a new approach has been considered to test the surrogate functions' suitability in fitting the optimum solutions. To this end, the optimum values of variables ( $x_1$  to  $x_5$ ) are imported to the finite element code and the corresponding results are illustrated in Figs. 10 and 11. The results indicate that the SEA optimum values based on Kriging, RSM, and FNN functions are greater than the RNN method, however, the RNN method has the minimum NMSE in training points.

#### 4.2.2 Single-objective optimization for PCF

To minimize the PCF, the single-objective optimization is performed in a manner similar to Section 4.2.1, and the

Table 7 MSE and NSME of SEA surrogate models

Metamodel	MSE	NMSE
Kriging	$1.24 \times 10^{-29}$	$1.61 \times 10^{-27}$
RNN	$1.05 \times 10^{-29}$	$1.37 \times 10^{-27}$
FNN	$77 \times 10^{-4}$	1
RSM	$2 \times 10^{-3}$	$2.60 \times 10^{-1}$

Table 8 MSE and NSME of PCF surrogate models

Metamodel	MSE	NMSE
Kriging	$2.73 \times 10^{-29}$	$1.58 \times 10^{-27}$
RNN	$2.84 \times 10^{-30}$	$1.65 \times 10^{-28}$
FNN	$1.72 \times 10^{-2}$	1
RSM	$0.78 \times 10^{-2}$	$4.53 \times 10^{-1}$

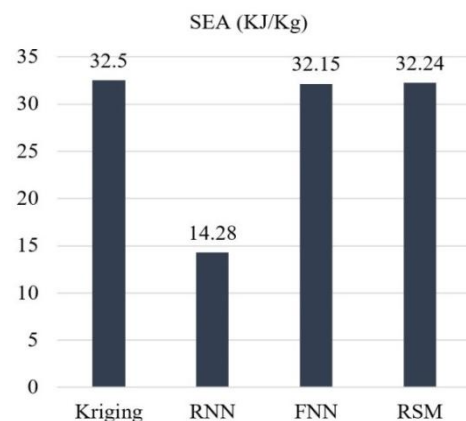


Fig. 10 SEA optimum values of surrogate models

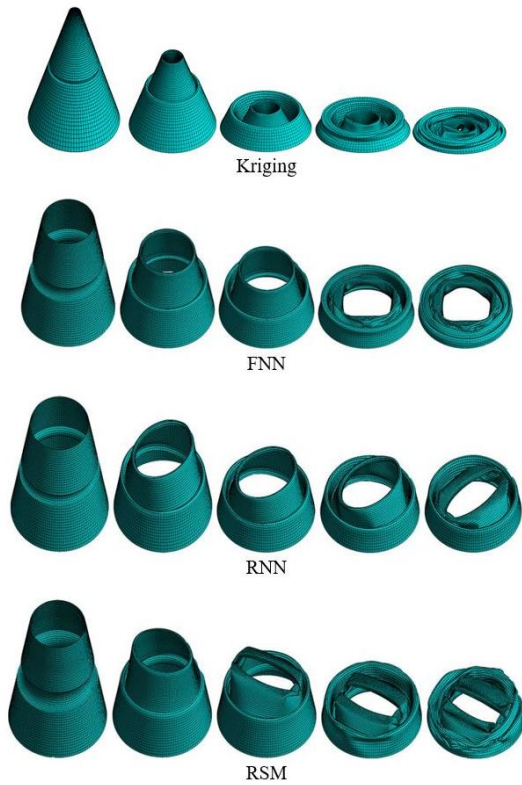


Fig. 11 FE deformed shapes of SEA optimum points

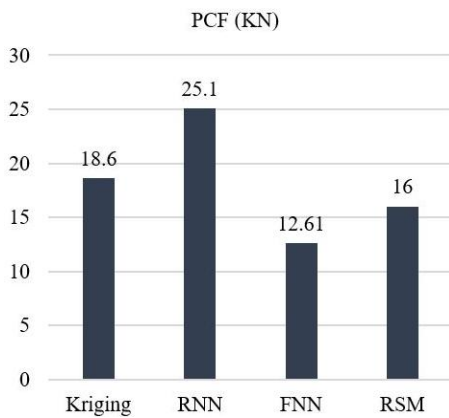


Fig. 12 PCF optimum values of surrogate models

optimum results are shown in Fig. 12. Results indicate that the PCF optimum values based on FNN function is less than the other surrogate models; however, the FNN has the maximum NMSE in training points. The finite element deformed shapes of the PCF optimum point are shown in Fig. 13.

#### 4.2.3 Multi-objective optimization for PCF and SEA

In this paper, the energy absorption capacity and the peak crushing force are optimized simultaneously. To this end, multi-objective optimization with the mentioned constraints in Section 4.2.1 is carried out as follows

$$\begin{aligned} &\text{Find} && x = (H, R, t, \alpha, r) \\ &\text{Minimize} && f = \{f_1 = -SEA(x) \text{ and } f_2 = PCF(x)\}. \end{aligned}$$

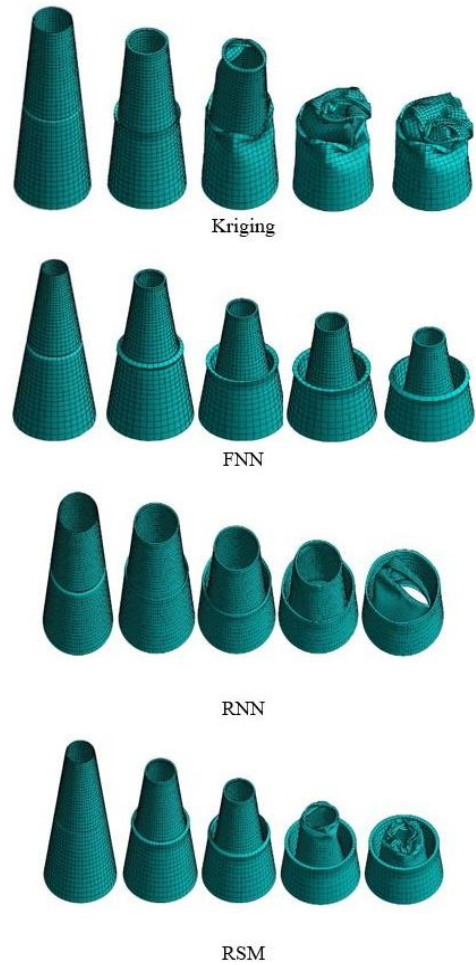


Fig. 13 Finite element deformed shapes of PCF optimum points

Based on the NSGA-II, the Pareto points are evaluated to solve the multi-objective optimization problem. The last generation of multi-objective optimization in each of the meta-models are shown in Fig. 14.

From Fig. 14, three candidate points of RSM, FNN and RNN-based multi-objective optimization have been chosen as the samples of optimum solutions ( $A_i, B_i, C_i$ ). Herein,  $i = 1, 2, 3$  denotes to the RSM, FNN and RNN, respectively. These points are implemented in finite element code and the values of the SEA and the PCF are shown in Table 9. Deformed shapes of RSM candidate points ( $A_1, B_2, C_3$ ) have been shown in Fig. 15.

#### 4.2.4 Optimization of indentation's shape

In this section, to investigate the effect of the indentation's shape on the crushing behaviour of energy absorbers, triangular, squared, hexagonal, and circular indentation shapes are considered. To this end, similar tube geometries ( $t = 2 \text{ mm}, \alpha = 85, R = 75, H = 180 \text{ mm}$ ) with the mentioned shapes of indentation have been modelled in the finite element code. According to the Figs. 16 and 17, the SEA and the PCF values for the shapes of indentation and the force-displacement curves are illustrated, respectively.

As shown in Figs. 16 and 17, the PCF value of the

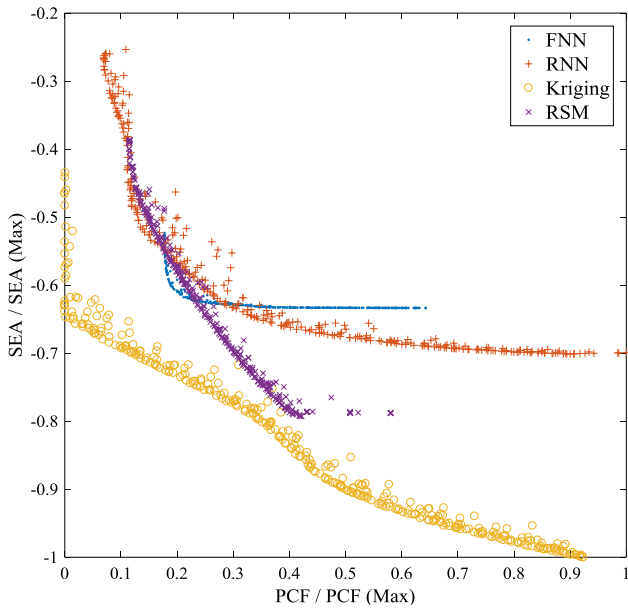


Fig. 14 Last generation of surrogate based multi-objective optimization



Fig. 15 Finite element deformed shapes of RSM candidate points  $A_1$ ,  $B_2$  and  $C_3$

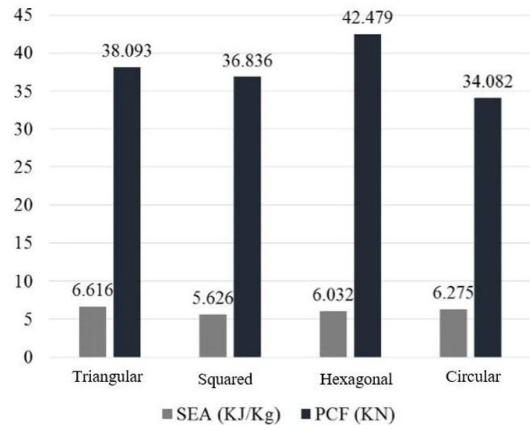


Fig. 16 SEA and PCF values based on indentation's shapes

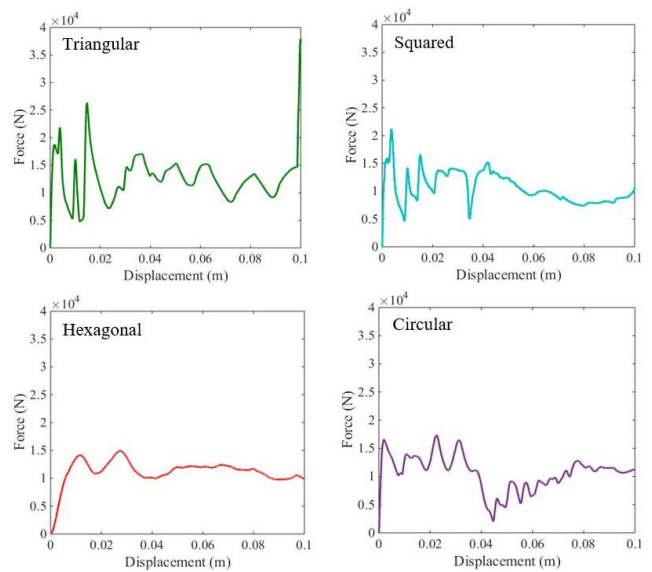


Fig. 17 Force-displacement curves based on the indentation's shape

hexagonal shape is greater than the other shapes, possessing a smoother fluctuation of the force-displacement curve in comparison. In addition, the SEA value of the triangular

Table 9 Candidate points of RSM, FNN and RNN-based multi-objective optimization

Meta-model	Pareto point	$x_1$ (mm)	$x_2$ (mm)	$x_3$ (mm)	$x_4$ (°)	$x_5$ (mm)	Mass (kg)	Metamodel		FEM model		
								PCF (kN)	SEA (kJ/kg)	PCF (kN)	SEA (kJ/kg)	Plastic energy (J)
RSM	$A_1$	283.54	100.96	0.52	78.26	2.13	0.184	10.00	5.53	13.75	4.08	751.26
	$B_1$	279.88	100.77	0.51	78.21	2.12	0.178	10.01	5.60	13.51	4.40	786.30
	$C_1$	282.95	103.72	0.52	78.19	2.11	0.190	10.06	5.41	13.82	4.00	763.14
FNN	$A_2$	259.96	66.32	0.5	80.51	8.13	0.102	17.71	8.45	17.14	7.85	801.85
	$B_2$	249.4	68.17	0.5	81.12	8.24	0.106	18.52	8.39	18.53	8.09	865.88
	$C_2$	246.47	66.54	0.5	80.2	7.8	0.098	17.88	8.48	17.58	9.12	898.17
RNN	$A_3$	251.65	96.06	0.61	78.2	7.35	0.190	17.18	6.41	17.03	5.73	1093.50
	$B_3$	262.15	67.8	0.61	80.33	4.51	0.127	9.79	5.70	11.63	6.25	795.71
	$C_3$	253.61	86.34	0.55	78.73	7.38	0.151	15.22	6.98	14.02	6.27	948.50

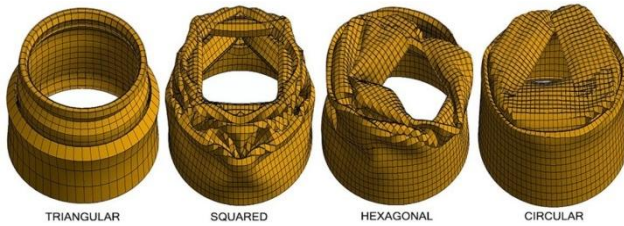


Fig. 18 Finite element deformed shapes of tapered tube for indentation shapes

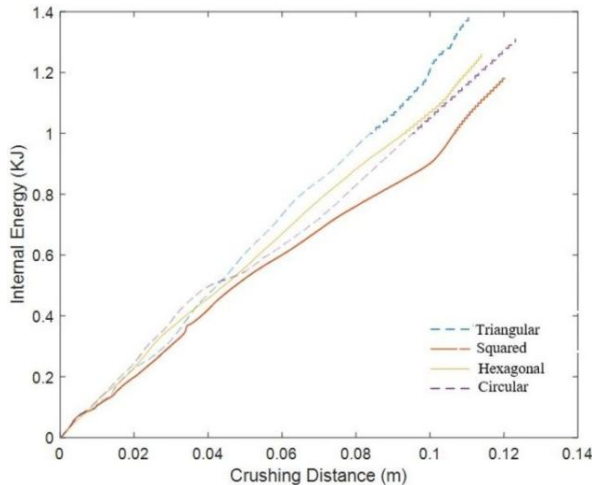


Fig. 19 Variation of internal energy versus crushing distance for indentation's shapes

shape is higher than the other indentations shapes because of the symmetric crushing mode that occurs during impact loading. The circular shape of indentation has the smallest value of the PCF because it leads to a diamond three-lobe crushing mode. The finite element deformed shapes of the tapered tube with different indentation shapes are illustrated in Fig. 18. A better understating of force-displacement curves can be obtained from internal energy-displacement curves, which are depicted in Fig. 19. It should be noted that ignoring geometrical perturbation, numerical methods only predict the axisymmetric collapsing mode while considering the effect of the imperfection, the crushing mode would be axisymmetric. (Baykasoglu and Cetin 2015).

## 5. Conclusions

In the present study, optimization of indented conical thin-walled tubes considering comparison between four metamodels including Kriging, the Feed Forward Neural Network (FNN), the Radial Basis Neural Network (RNN), and the 2nd order Response Surface Method (RSM) have been investigated. The model has been validated based on two theoretical solutions as well as an experimental test. Evolutionary algorithms (Genetic Algorithm (GA) and Non-dominated Sorting Genetic Algorithm (NSGA-II)) have been utilized for single- and multi-objective optimization procedures. In addition, with regard to the importance of

crushing modes in predicting the folding mechanism, the effect of indentation's shape on crushing has been investigated. The main results can be summarized as follows:

- Based on the RSM coefficients, thickness, tapered radius, and height are important variables for specific energy absorption (SEA). Meanwhile, thickness is an effective design variable for the peak crushing force (PCF), especially when it is considered concurrently with design variables including tapered angle and tapered radius.
- In the single-objective optimization problems, the RNN method has the lowest NMSE in training sample points while it does not exhibit a good fit with optimum points (with a lower value of 125.7% for SEA and a higher value of 56.8% for PCF).
- In terms of SEA (single-objective optimization), the Kriging, the FNN and the RSM methods exhibit almost a similar fitting on optimum points, however, the Kriging method shows a lower MSE than the other two methods (error order of  $10^{-29}$ ).
- In the single-objective optimization for the PCF, the FNN method shows a better fitting on optimum points in comparison with the other three methods (49% lower than the RNN method).
- Indentation shape plays an essential role in crushing characteristics (SEA and PCF) and can lead to different crushing modes. It is also concluded that the triangular shape of indentation can lead to an axisymmetric crushing mode and increase the value of SEA by 17.6%. Moreover, the circular shape of indentation minimizes the PCF by 24.6%, leading to a three-lobe diamond mode.

## References

- Abramowicz, W. and Jones, N. (1984), "Dynamic axial crushing of square tubes", *Int. J. Impact Eng.*, **2**(2), 179-208.
- Acar, E., Guler, M.A., Gerçeker, B., Cerit, M.E. and Bayram, B. (2011), "Multi-objective crashworthiness optimization of tapered thin-walled tubes with axisymmetric indentations", *Thin-Wall. Struct.*, **49**(1), 94-105.
- Ambrosio, J.A.C. (2001), *Crashworthiness*, Springer-Verlag Wien.
- Azimi, M.B. and Asgari, M. (2016a), "A new bi-tubular conical-circular structure for improving crushing behavior under axial and oblique impacts", *Int. J. Mech. Sci.*, **105**, 253-265.
- Azimi, M.B. and Asgari, M. (2016b), "Energy absorption characteristics and a meta-model of miniature frusta under axial impact", *Int. J. Crashworth.*, **21**(3), 222-230.
- Baroutaji, A., Gilchrist, M., Smyth, D. and Olabi, A.-G. (2015), "Crush analysis and multi-objective optimization design for circular tube under quasi-static lateral loading", *Thin-Wall. Struct.*, **86**, 121-131.
- Baykasoglu, A. and Baykasoglu, C. (2016), "Crashworthiness optimization of circular tubes with functionally-graded thickness", *Eng. Computat.*, **33**(5), 1560-1585.
- Baykasoglu, A. and Baykasoglu, C. (2017), "Multiple objective crashworthiness optimization of circular tubes with functionally graded thickness via artificial neural networks and genetic algorithms", *Proceedings of the Institution of Mechanical Engineers, Part C: Journal of Mechanical Engineering Science*,

- 231(11), 2005-2016.
- Baykasoglu, C. and Cetin, M.T. (2015), "Energy absorption of circular aluminium tubes with functionally graded thickness under axial impact loading", *Int. J. Crashworth.*, **20**(1), 95-106.
- Esfahlani, S.S., Shirvani, H., Shirvani, A., Nwaubani, S., Mebrahtu, H. and Chirwa, C. (2013), "Hexagonal honeycomb cell optimisation by way of meta-model techniques", *Int. J. Crashworth.*, **18**(3), 264-275.
- Fang, J., Sun, G., Qiu, N., Kim, N.H. and Li, Q. (2017), "On design optimization for structural crashworthiness and its state of the art", *Struct. Multidiscipl. Optimiz.*, **55**(3), 1091-1119.
- Gu, X., Dai, J., Huang, X. and Li, G. (2017), "Reliable optimisation design of vehicle structure crashworthiness under multiple impact cases", *Int. J. Crashworth.*, **22**(1), 26-37.
- Guler, M.A., Cerit, M.E., Bayram, B., Gerçeker, B. and Karakaya, E. (2010), "The effect of geometrical parameters on the energy absorption characteristics of thin-walled structures under axial impact loading", *Int. J. Crashworth.*, **15**(4), 377-390.
- Gupta, N.K., Sheriff, N.M. and Velmurugan, R. (2006), "A study on buckling of thin conical frusta under axial loads, Thin-Walled Structures", **44**(9), 986-996.
- Hanssen, A.G., Langseth, M. and Hopperstad, O.S. (2000), "Static and dynamic crushing of circular aluminium extrusions with aluminium foam filler", *Int. J. Impact Eng.*, **24**(5), 475-507.
- Hosseinipour, S.J. and Daneshi, G.H. (2003), "Energy absorption and mean crushing load of thin-walled grooved tubes under axial compression", *Thin-Wall. Struct.*, **41**(1), 31-46.
- Khalkhali, A. and Samareh Mousavi, S. (2012), "Multi-objective Crashworthiness Optimization of the Aluminum Foam-filled Tubes", *Int. J. Automot. Eng.*, **2**(3), 193-206.
- Khayat, M., Poorveis, D. and Moradi, S. (2017), "Buckling analysis of functionally graded truncated conical shells under external displacement-dependent pressure", *Steel Compos. Struct., Int. J.*, **23**(1), 1-16.
- Kim, S.K., Hwang, K.H.I.C.S. and Yang, I.Y. (2002), "A Study on Experimental Characteristics of Energy Absorption Control in Thin-Walled Tubes for the Use of Vehicular Structure Members", *Int. J. Automot. Technol.*, **3**(4), 137-145.
- Koziel, S., Ciaurri, D.E. and Leifsson, L. (2011), *Surrogate-Based Methods*, Springer Berlin Heidelberg, Berlin, Heidelberg, Germany.
- Lophaven, S.N., Nielsen, H.B. and Søndergaard, J. (2002), *DACE-A MATLAB Kriging Toolbox*, Technical University of Denmark, Lyngby, Denmark.
- MacLeod, C. (2010), *An Introduction to Practical Neural Networks and Genetic Algorithms For Engineers and Scientists*, The Robert Gordon University.
- Mahmoodi, A., Shojaeefard, M.H. and Saeidi Googarchin, H. (2016), "Theoretical development and numerical investigation on energy absorption behavior of tapered multi-cell tubes", *Thin-Wall. Struct.*, **102**, 98-110.
- Mamalis, A., Manolacos, D., Ioannidis, M. and Kostazos, P. (2005), "Numerical simulation of thin-walled metallic circular frusta subjected to axial loading", *Int. J. Crashworth.*, **10**(5), 505-513.
- Marzbanrad, J., Abdollahpoor, A. and Mashadi, B. (2009), "Effects of the triggering of circular aluminum tubes on crashworthiness", *Int. J. Crashworth.*, **14**(6), 591-599.
- Myers, R.H., Montgomery, D.C. and Anderson-Cook, C.M. (2009), *Response Surface Methodology: Process and Product Optimization Using Designed Experiments*, Wiley.
- Nagel, G. (2005), *Impact and Energy Absorption of Straight and Tapered Rectangular Tubes*, Queensland University of Technology, Brisbane, Australia.
- Najafi, A. (2009), *Axial Collapse of Thin-walled, Multi-corner Single-and multi-cell Tubes*, Mississippi State University, Starkville, MS, USA.
- Park, J.-S. (1994), "Optimal Latin-hypercube designs for computer experiments", *J. Statist. Plan. Infer.*, **39**(1), 95-111.
- Qi, C., Yang, S. and Dong, F. (2012), "Crushing analysis and multiobjective crashworthiness optimization of tapered square tubes under oblique impact loading", *Thin-Wall. Struct.*, **59**, 103-119.
- The ANSYS Inc. (2009), ANSYS user's guide and reference guide.
- Vinayagar, K. and Senthil Kumar, A. (2017), "Multi-response optimization of crashworthiness parameters of bi-tubular structures", *Steel Compos. Struct., Int. J.*, **23**(1), 31-40.
- Wallis, W.D. and George, J.C. (2010), *Introduction to Combinatorics*, CRC Press.
- Zarei, H.R. and Kröger, M. (2006), "Multiobjective crashworthiness optimization of circular aluminum tubes", *Thin-Wall. Struct.*, **44**(3), 301-308.
- Zhang, X. and Huh, H. (2009), "Energy absorption of longitudinally grooved square tubes under axial compression", *Thin-Wall. Struct.*, **47**(12), 1469-1477.
- Zhang, X., Cheng, G., You, Z. and Zhang, H. (2007), "Energy absorption of axially compressed thin-walled square tubes with patterns", *Thin-Wall. Struct.*, **45**(9), 737-746.
- Zhang, Z., Liu, S. and Tang, Z. (2010), "Crashworthiness investigation of kagome honeycomb sandwich cylindrical column under axial crushing loads", *Thin-Wall. Struct.*, **48**(1), 9-18.
- Zhang, Y., Sun, G., Xu, X., Li, G. and Li, Q. (2014), "Multiobjective crashworthiness optimization of hollow and conical tubes for multiple load cases", *Thin-Wall. Struct.*, **82**, 331-342.

CC

**Appendix A. Design of experiments**

Design of experiments is a well-established and rigorous approach to engineering problems that applies principles and techniques at the design space so as to generate interpreting sets of experiment that ensure validity and reliability of engineering conclusions. Many types of DOE have been utilized during the increasingly growth of engineering concerns including full factorial, fractional factorial, central composite designs, Box-Behnken and Latin Hypercube sampling (LHS). First step in LHS method is to specify number of sample points then divide the design space and put sample points into divisions based on Latin Square method which was inspired by Euler (Wallis and George 2010). LHS sample points for FNN, RNN and Kriging are shown in the following table (Table A1).

Table A1 Sample points based on Latin Hypercube sampling method

Number	H	R	t	α	r
1	151.52	147.42	2.8	83.94	4.34
2	139.39	123.18	1.99	84.55	7.09
3	290.91	130.45	1.61	67.84	6.69
4	239.39	177.73	1.54	63.94	9.6
5	354.55	78.33	1.28	79.54	3.62
6	209.09	131.67	2.14	76.67	2.32
7	327.27	137.73	1.03	90	5.39
8	145.45	68.64	1.96	79.09	4.67
9	227.27	165.61	2.27	60.3	2.97
10	318.18	134.09	1.91	89.39	9.19
11	324.24	109.85	2.09	73.28	9.92
12	112.12	160.76	1.26	72.12	2.4
13	175.76	75.91	1.08	85.45	6.53
14	212.12	108.64	2.65	64.88	8.71
15	336.36	81.97	2.6	86.36	8.55
16	166.67	121.97	1.79	61.21	5.07
17	393.94	124.39	2.17	76.97	7.82
18	136.36	185	2.7	65.15	8.79
19	375.76	149.85	0.9	72.73	2.57
20	269.7	120.76	2.55	87.27	3.7
21	293.94	145	2.77	75.76	5.56
22	263.64	73.48	1.36	76.42	8.95
23	215.15	171.67	1.16	77.88	9.84
24	378.79	159.55	1.74	68.48	9.27
25	230.3	83.18	2.12	88.48	6.28
26	369.7	161.97	0.78	69.09	7.01
27	203.03	166.82	1.43	67.88	5.96
28	233.33	125.61	2.72	81.52	8.22
29	372.73	97.73	2.07	85.15	5.23
⋮					
99	309.09	98.94	1.59	79.7	9.76
100	169.23	185	1.94	72.69	7.54

**Appendix B. Surrogate models**

*B.1 Response surface methodology*

For the determination of C matrix of coefficient the linear algebraic operations are applied. Overall form of 2<sup>nd</sup> order RSM are as followed in which f is predicting response function and x is design variables vector, x<sub>i</sub> is design variables and l is the number of design variables (Myers et al. 2009).

$$f(X) = C_0 + \sum_{i=1}^l C_i x_i + \sum_{i=1}^l C_{ii} x_i^2 + \sum_{i=1}^{l-1} \sum_{j=i+1}^l C_{ij} x_i x_j \quad (B1)$$

$$x = [x_1 x_2 x_3 \dots x_l]$$

In order to follow up the procedure it is required to make a response matrix y with the dataset taken by DOE in which the y<sub>i</sub> corresponds to response of ith design vector.

$$y = \begin{bmatrix} y_{1th \ response} \\ y_{2ed \ response} \\ \vdots \end{bmatrix} \quad (B2)$$

$$U = [1 \ x_1 x_2 \ \dots \ x_1^2 x_2^2 \ \dots \ x_1 x_2 \ \dots \ x_1 x_3 \ \dots \ ]$$

$$C = (U'U)^{-1} U' y$$

*B.2 Radial basis neural network*

In this method the procedure of training is conducted in the following two levels. Level one is considered for the calculation of weights through input layers and hidden layers. In the second level corresponding to the calculated weights, the new connecting weights between hidden layers and outputs, should be obtained. The Radial function of Neural Network f(x) is mentioned as follows (MacLeod 2010)

$$f(x) = \sum_{i=1}^l w_i \phi(r) \quad (B3)$$

$$r = \|x - c_i\|$$

in which c<sub>i</sub> are first layer weights, w<sub>i</sub> are connection weights from hidden layer to output, φ is activation function that should be radially symmetric.

*B.3 Kriging method*

In Kriging method, the main structure is based on the 1st or 2nd order polynomial which completely predicts such as the response surface method. The residual part of Kriging functions Z, is more complicated than the main part, and is based on Gaussian random distribution with zero value of mean and non-zero values of variance and covariance, which are defined as follows

$$Cov[Z(x^i)Z(x^j)] = \sigma^2 R ([R(x^i), x^j]) \quad (B4)$$

In the equation, R is variables correlation and R(x<sup>i</sup>, x<sup>j</sup>) is correlation function through two sample points x<sup>i</sup> and x<sup>j</sup>. In this study, the correlation function is assumed as Gaussian distribution (Koziel et al. 2011).